Microstructure and Mechanical Properties of 1,000 MPa Ultra-High Strength Hot-Rolled Plate Steel for Coal Mine Refuge Chamber

Changsheng Li · Biao Ma · Tao Li · Tao Zhu

Abstract The 1,000 MPa ultra-high strength hot-rolled plate steel with low-carbon bainitic microstructure was developed in the laboratory for coal mine refuge chamber. The static recrystallization behavior, microstructure evolution, and mechanical properties of this hot-rolled plate steel were investigated by the hot compression, continuous cooling transformation, and tensile deformation test. The results show that the developed steel has excellent mechanical properties at both room and elevated temperature, and its microstructure mainly consists of lath bainite, granular bainite, and ferrite after thermal–mechanical control process (TMCP). The ultra-high strength plate steel is obtained by the TMCP process in hot rolling, strengthened by bainitic transformation, microstructure refinement, and precipitation of alloying elements such as Nb, Ti, Mo, and Cu. The experimental steel has relatively low welding crack sensitivity index and high atmospheric corrosion resistance index. Therefore, the developed steel has a good balance of strength and ductility both at room and elevated temperature, weldability and corrosion resistance, and it can suffice for the basic demands for materials in the manufacture of coal mine refuge chamber.

KEY WORDS: Ultra-high strength steel; Low-carbon bainite; Coal mine refuge chamber; Microstructure; Mechanical property

1 Introduction

As safety facilities have been gradually required for coal mines in recent years, refuge chambers are always applied to provide safety room for the miners who are suffering from catastrophic emergencies, such as overbreak, gas explosion, and mine flood. In view of complex work surroundings in coal mines, the plate steel for application in refuge chambers should possess a good combination of high weldability [1, 2], corrosion resistance [3, 4], high temperature resistance, high strength and ductility [5, 6].

Generally, the manufacture of the refuge chamber body prefers to employ the plain carbon steels or high strength low alloy steels for the reason that the yield strength was about 235–600 MPa and other mechanical properties like ductility and cold bending could also satisfy the requirements narrowly. However, these ordinary steels may reveal their shortcomings in the corrosion and heat resistance more clearly due to the influence of high temperature airflow generated by gas explosion and corrosive gas (i.e., methane, hydrogen sulfide, et al.). Therefore, the development of customized steels having superior comprehensive properties is critical to manufacture the coal mine refuge chambers.

The investigation on structural steels for coal mines in China was sluggish and still remained a lower level. Since the 16Mn steel was developed in the early of 1960s, a series of new types of steels including 15MnMoNb steel have been widely applied in the national economic

C. Li (✉) · B. Ma · T. Li · T. Zhu
State Key Laboratory of Rolling and Automation, Northeastern University, Shenyang 110819, China
e-mail: lics@ral.neu.edu.cn

construction. Due to the limitation of alloying elements and production condition, the metallurgical quality of these plate steels was poor. Besides, the plasticity and ductility became quite low and their properties were also unstable with the strength level enhanced. Hence, there was a broad gap between these domestic types of steels and the same foreign products.

As a result of the progress in steel making and thermal–mechanical control process (TMCP) techniques, low-carbon bainitic steels have become the prior direction for the development of high strength steels. They usually have high strength, good ductility, and machinability [7]. Because of the extremely low-carbon content in these steels, the negative effect of carbon on ductility is completely removed and fine bainitic laths with a high density of dislocations can be obtained by means of TMCP process [8, 9]. The guarantee of high strength is no longer dependent on the considerable carbon content but on the strengthening of grain refinement, dislocation substructures, and precipitation of alloying elements including Nb, V, Ti, and ε-Cu. Thus, the steel can achieve a good weldability and resistance to hydrogen-induced cracking, in addition to superior combination of strength and ductility [10, 11].

The aim of this paper is to develop a 1,000 MPa grade low-carbon bainitic steel for coal mine refuge chamber in the laboratory. The static recrystallization behavior was analyzed and the continuous cooling transformation (CCT) test was also conducted, in order to guide the process of hot rolling and cooling. The effects of TMCP process parameters on microstructure evolution and mechanical properties of the hot-rolled steel were investigated. The present work is expected to provide a theoretical basis for the development and industrial application of ultra-high strength steel in coal mine refuge chamber.

2 Experimental

In consideration of the effects of individual elements on values of welding crack sensitivity index (P_{cm}) and the atmospheric corrosion resistance index (I), the designed chemical composition (wt%) of the experimental steel contains 0.03–0.05 C, 0.2–0.35 Si, 1.7–1.9 Mn, ≤0.01 P, ≤0.01 S, 0.2–0.35 Cu, 0.2–0.4 Mo, 0.3–0.5 Cr, 0.01–0.02 Ti, 0.04–0.06 Nb, 0.01–0.05 Al, 0.001–0.002 B, and balance of Fe.

The chemical composition (wt%) measured in the experimental steel contains 0.0495 C, 0.345 Si, 1.75 Mn, 0.007 P, 0.008 S, 0.323 Cu, 0.317 Mo, 0.427 Cr, 0.0183 Ti, 0.0556 Nb, 0.045 Al, 0.0017 B, and balance of Fe.

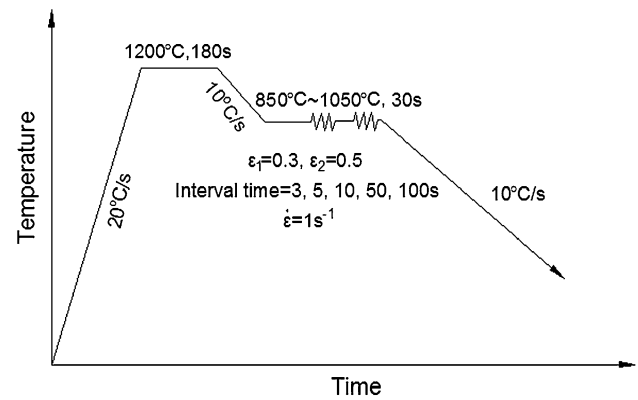The values of P_{cm} and I can be calculated as follows [12, 13]:

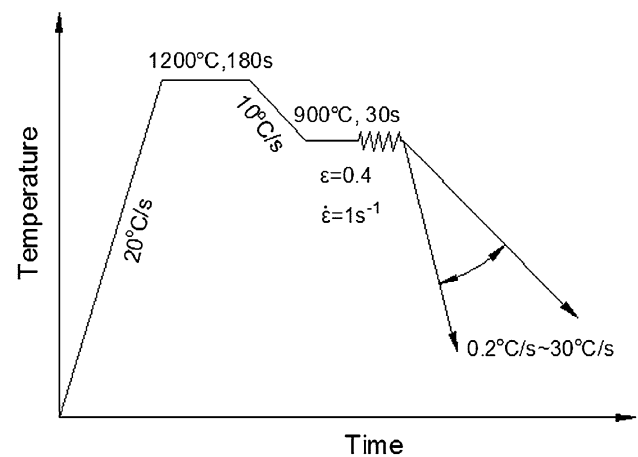**Fig. 1** The schematic diagram of double pass compression tests of the experimental steel

Fig. 2 The schematic diagram for CCT schedule of the experimental steel

$$P_{cm} = C_C + C_{Si}/30 + (C_{Mn} + C_{Cu} + C_{Ni})/60 + C_{Cr}/20 + C_{Mo}/15 + C_V/10 + 5C_B, \tag{1}$$

$$I = 26.01(C_{Cu}) + 3.88(C_{Ni}) + 1.20(C_{Cr}) + 1.49(C_{Si}) + 17.28(C_P) - 7.29(C_{Cu})(C_{Ni}) - 9.10(C_{Ni})(C_P) - 33.39(C_{Cu})^2, \tag{2}$$

where C is the content of the element which is mentioned by the subscript, in wt%. In general, $P_{cm} \leq 0.2\%$ and $I \geq 3$ are considered to meet the basic demands of weldability and corrosion resistance, respectively, for the application of the steel. The calculated values of P_{cm} and I of the experimental steel are 0.146% and 6.06, according to Eqs. (1) and (2), which indicates that it is able to suffice for the demands above mentioned.

Table 1 The actual TMCP parameters of the experimental steel

Processes	Initial rolling temperature (°C)	Finish rolling temperature (°C)	Initial cooling temperature (°C)	Finish cooling temperature (°C)	Cooling rate (°C/s)
R1	1,057	976	935	525	42
R2	1,100	946	882	502	42
R3	1,040	910	886	616	34
R4	1,034	913	890	Air cooled	Air cooled

The samples for hot compression were machined into cylindrical rods with a size of $\Phi 8\,\text{mm} \times 15\,\text{mm}$. The schemes of double pass compression and CCT tests are shown in Figs. 1 and 2, respectively.

The billets were austenitized for 2 h at 1,200 °C and then hot rolled for five passes with a thickness reduction from 40 to 3 mm. In Table 1, R1–4 represent the four processes of TMCP, respectively. Process parameters of TMCP are including initial rolling temperature, finish rolling temperature, initial cooling temperature, finish cooling temperature, cooling time, and cooling rate.

The double pass compression test and CCT test were carried out by the MMS-300 thermomechanical simulator. The hot-rolling experiment was conducted by a $\Phi 450\,\text{mm}$ trial rolling mill with an ICON portable infrared thermometer used for temperature measurement. The microstructure of the samples was observed by LEICA-DMIRM optical microscopy. The tensile tests were performed with the aid of CMT5105 universal tensile testing machine at room temperature and 500 °C. The Charpy impact test was conducted using an INSTRON 9250HV Instrumented impact testing machine. The impact samples with a dimension of 55 mm × 10 mm × 2.5 mm were cut along the rolling direction. In addition, the FEI Quanta 600 scanning electron microscopy (SEM) was further applied to analyze the metallographic structure of the hot-rolled steels and the fracture surface of Charpy V-notch samples. The detailed observation of bainitic substructures and precipitation was achieved by FEI Tecnai G^2 F20 transmission electron microscopy (TEM).

3 Results and Discussion

3.1 Static Recrystallization Behavior

The activation energy of static recrystallization is generally defined using the time $t_{0.5}$ for recrystallization fraction of 50%, which can be calculated from the following relation [14, 15]:

$$t_{0.5} = A\varepsilon^p\dot{\varepsilon}^q D^s \exp(Q/RT), \tag{3}$$

where the parameters of A, p, q and s are constants, Q represents the activation energy of static recrystallization (kJ/mol), D is the diameter of austenite (A) grains, and T is the thermodynamic temperature.

The slope Q/R of the fitted line is 48,196.6 mol/K based on the experimental data of double pass compression tests. Thus, the activation energy of static recrystallization for the steel is 400.9 kJ/mol.

Generally, the static recrystallization kinetics of A follows the Avrami equation [16–18]:

$$X_s = 1 - \exp[-0.693(t/t_{0.5})^n], \tag{4}$$

where X_s is the percentage of static recrystallization and determined by the relationship $X_s = (F_{s1} - 0.8)/0.2$ and the curves of softening ratio, and n is a parameter associated with deformation.

After taking the natural logarithm twice, the Eq. (4) can be rewritten as

$$\ln \ln[1/(1 - X_s)] = \ln 0.693 + n\ln(t/t_{0.5}). \tag{5}$$

$\ln \ln[1 - (1 - X_s)]$ and $\ln(t/t_{0.5})$ are taken as y- and x-coordinate, respectively, and then linearly fitted using Origin software. Corresponding to different temperatures of 950, 1000, and 1050 °C, the deformation parameter n is 0.2622, 0.3346, and 0.5014, respectively.

3.2 Continuous Cooling Transformation Characteristics

The CCT diagram of the steel is shown in Fig. 3. The start and finish transformation temperatures are increased with increasing cooling rates. Especially the pearlite–ferrite transformation temperature is increased up to 700 °C in low cooling rates. In addition, the cooling rate range for the formation of granular bainite (GB) microstructure is enlarged so that it can be still formed despite the cooling rate of 25 °C/s. Accordingly, the martensite (M) transformation is fully suppressed under the cooling rate of 30 °C/s while the cooling rate range for lath bainite (LB) formation is also reduced.

A high cooling rate restrains the diffusion of C atoms and favors the occurrence of the shear transformation mechanism, resulting in the decrease of start
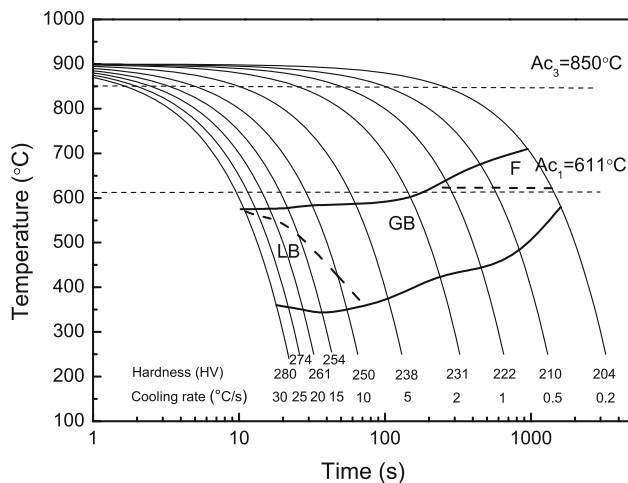
Fig. 3 The CCT diagram of the experimental steel

transformation temperature. The addition of Mo, Cr, Nb, B, and Ti suppresses the nucleation of polygonal ferrite (PF) at the prior A grain boundaries and promotes the GB and LB transformation [19, 20].

The formation of PF and GB is mainly controlled by the diffusion of C and Fe atoms. The hot deformation dramatically increases the grain boundary areas and the amount of deformation bands and dislocations inside the A grains, with the diffusion of C and Fe atoms accelerated. Therefore, the deformation improves the ferritic nucleation sites and also makes the sub-cooled A more unstable, leading to the enhancement of driving force for ferrite transformation. As a result, the start transformation temperatures for PF and GB are observably raised. Furthermore, the high density of dislocations inside the deformed A grains can inhibit the M transformation and the growth of LB and finally lead to the absence of M at the cooling rate of 30 °C/s [9, 21, 22].

3.3 Microstructure Evolution During TMCP Process

The optical micrographs of the steel plates with TMCP processes are presented in Fig. 4. The microstructure of steel at process R1 contains LB, GB, and small amounts of ferrite. The microstructure of steel at process R2 is mainly composed of LB and ferrite, while the steel at both R3 and R4 process has a microstructure of GB together with a similarly small amount of ferrite.

It is worth noting that the steel is directly air cooled to room temperature after hot rolling at process R4. According to the CCT curve of the tested steel, it is easy to obtain bainitic microstructure under a wide range of cooling rate. That is to say, the range of parameter control is enlarged during TMCP process. This is because the combined addition of Cr, Cu, Mo, and B makes the CCT curve move right so that the bainitic transformation can occur under quite a low cooling rate. Furthermore, the experimental steel has LB both at R1 and R2 processes. But the steel has fully LB microstructure at process R2 compared with R1, since lower initial and finish cooling temperatures are more beneficial to the LB formation.

Based on the microstructure of the steel in hot rolling, the low temperature phase transformation is favored with increasing cooling rate and decreasing finish cooling temperature. This is consistent with the transformation tendency in CCT diagram. However, the total reduction of hot rolling was about 92%, which was much larger than that used in CCT test. It can be deduced that the cooling rate range for GB transformation in practical hot rolling will be further enlarged due to the large reduction.

SEM micrographs of the steel plates with four different processes are shown in Fig. 5. From the figure, the microstructure of M–A can be observed. The steel has the fine M–A constituents with a smallest size at process R2, while M–A constituents of the steel at processes R3 and R4 are most coarse. These constituents are distributed in order and approximately parallel to the ferrite lath. The formation of finer LB in the steel at process R2 results from lower initial and finish cooling temperatures.

Figure 6 shows the TEM morphology of bainitic substructure and precipitation of the steel at process R2. As shown in Fig. 6a, the bainitic substructure is mainly composed of ferrite lath with a high density of dislocations. The width of M–A islands formed at the boundary of adjacent ferrite laths is about 0.3 μm. Further observations show that the substructure of M in M–A islands consists of
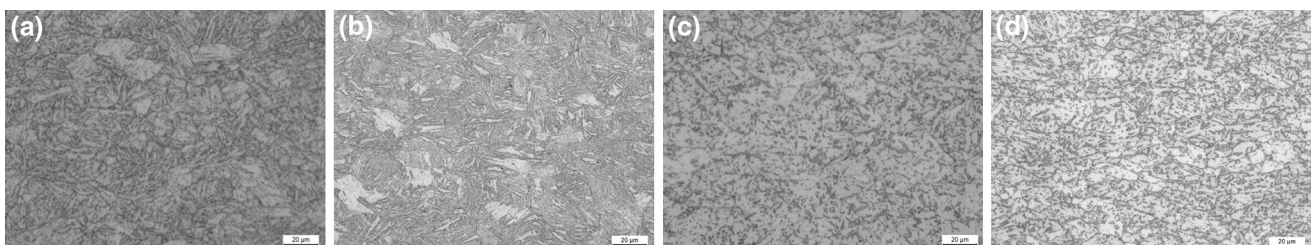

Fig. 4 Optical micrographs of the experimental steels at process R1 **a**, process R2 **b**, process R3 **c**, process R4 **d**
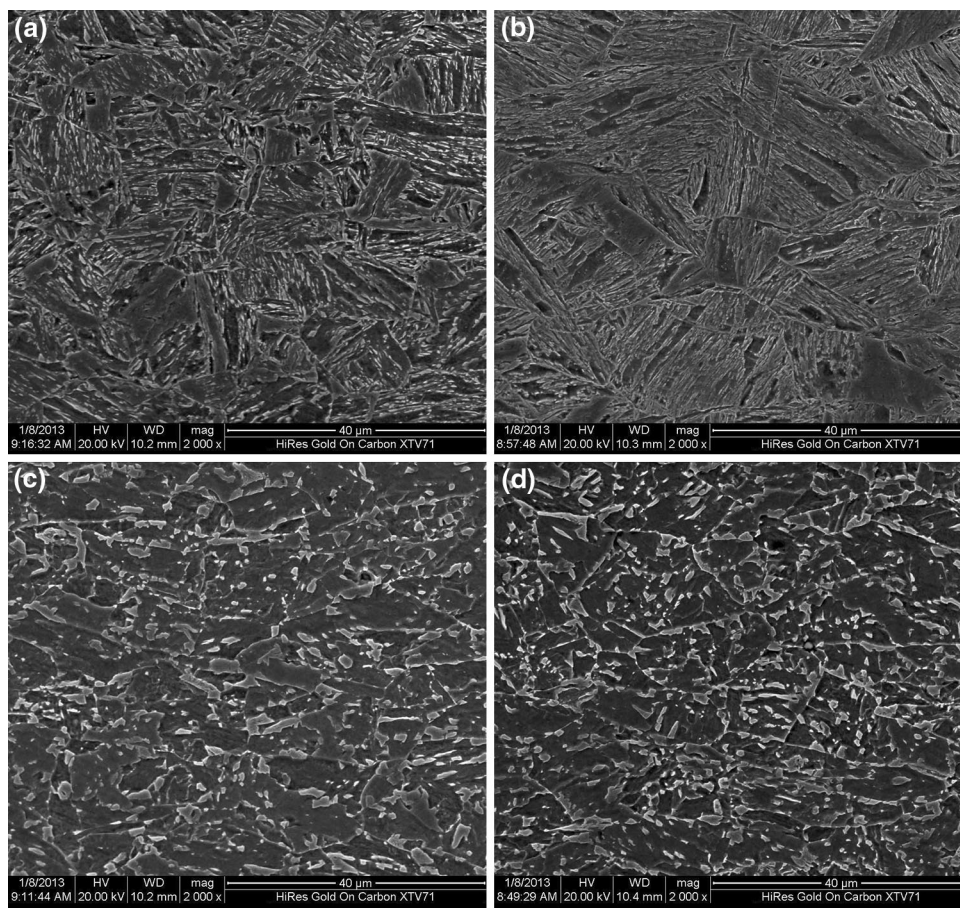
Fig. 5 SEM micrographs of the experimental steels at process R1 **a**, process R2 **b**, process R3 **c**, process R4 **d**
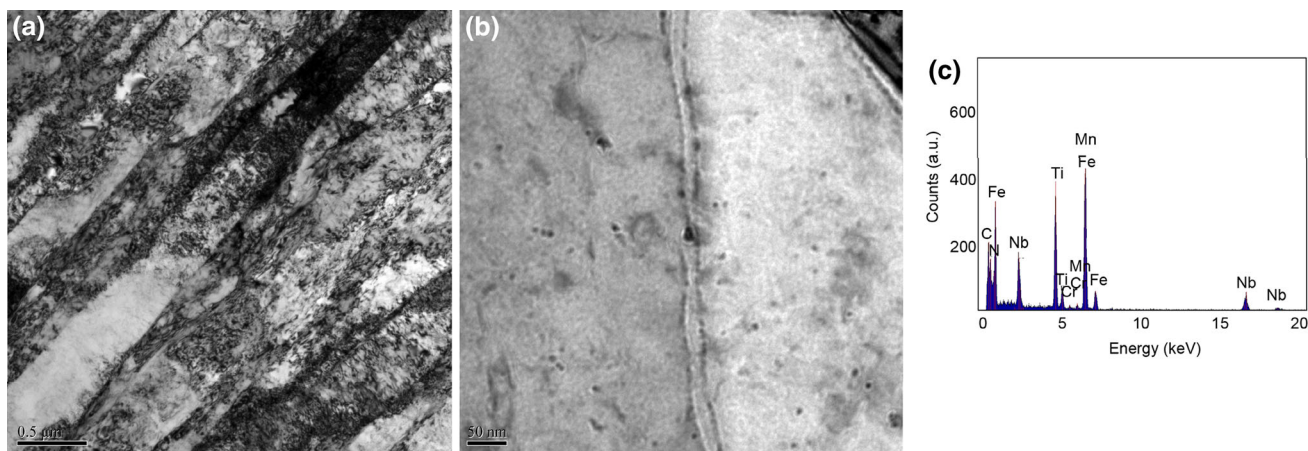

Fig. 6 TEM morphologies showing the bainitic substructure **a**, precipitates **b**, the EDS result of the precipitates in steel at process R2 **c**

carbon-enriched micro-twins. The average width of ferrite laths is 0.2–0.3 μm. Fine precipitated particles have a dispersive distribution on the ferrite laths, as shown in Fig. 6b. The energy spectrum of precipitates in the steel at process R2 is shown in Fig. 6c. It indicates that these particles are Nb/Ti carbonitrides. Due to the addition of Cu,

Table 2 The tensile properties of the steel at processes R1–4 at room temperature

Processes	Yield strength (MPa)	Tensile strength (MPa)	Elongation (%)	Yield ratio
R1	745	950	12.5	0.78
R2	850	1,020	11.6	0.83
R3	580	810	15.4	0.72
R4	640	830	13.6	0.77

Table 3 The tensile properties of the steel at processes R1–4 at 500 °C

| Processes	Yield strength (MPa)	Tensile strength (MPa)	Elongation (%)	Yield ratio
R1	660	820	16.7	0.8
R2	710	840	15.2	0.85
R3	520	702	18.2	0.74
R4	575	704	16.4	0.81

it is supposed that fine precipitates of Cu exist among these dispersively distributed secondary phase particles [23].

3.4 Characterization of Mechanical Behaviors

The tensile properties of the steel at room temperature and 500 °C are listed in Tables 2 and 3. For each process, the yield and tensile strengths remain a high level, while the elongation is not large enough at room temperature.

The relatively higher strength can be ascribed to the slightly higher Mn content, together with the combined effects of B and Mo. At process R2, the steel has the highest strength because LB microstructure has a high density of dislocations and fine M–A constituents which have a great effect on the improvement of strength for the steel plate. On the contrary, the parallel bainitic ferrite laths of LB microstructure result in the low plasticity of the steel.

As shown in Table 3, the strength of the steel still remains high, even at the temperature of 500 °C.
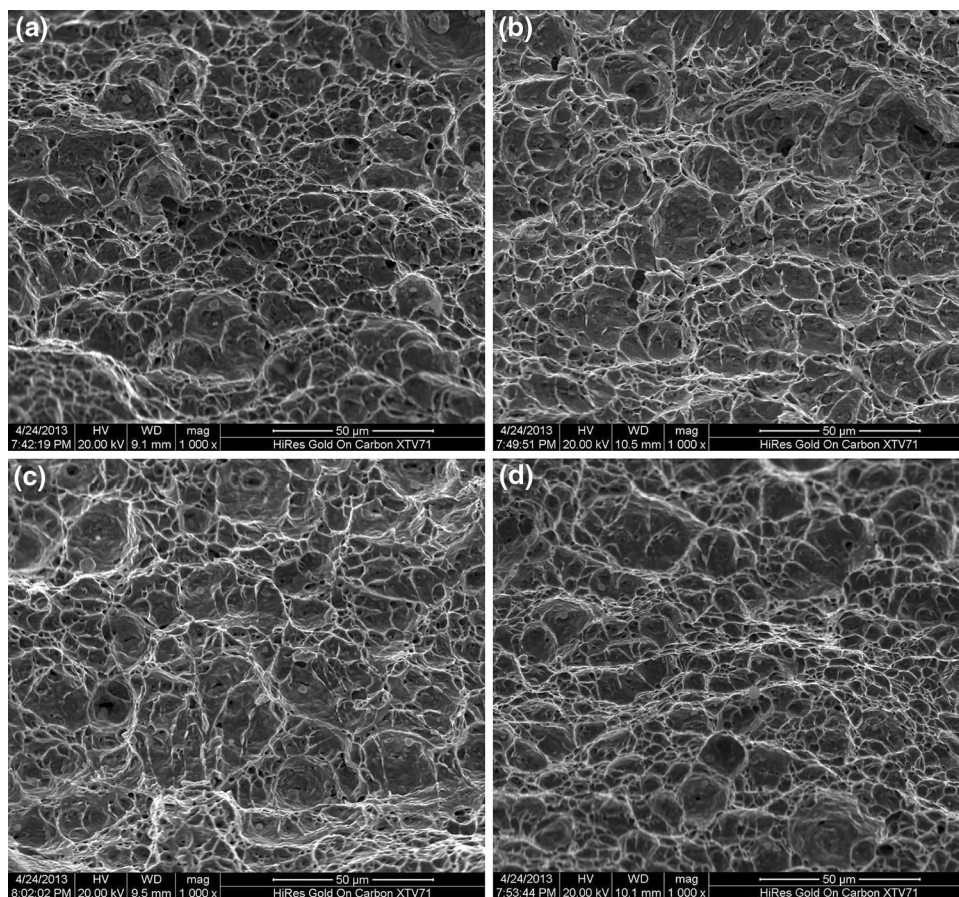
Fig. 7 The impact fracture morphology of the experimental steel at −20 °C with process R1 **a**, process R2 **b**, process R3 **c**, process R4 **d**
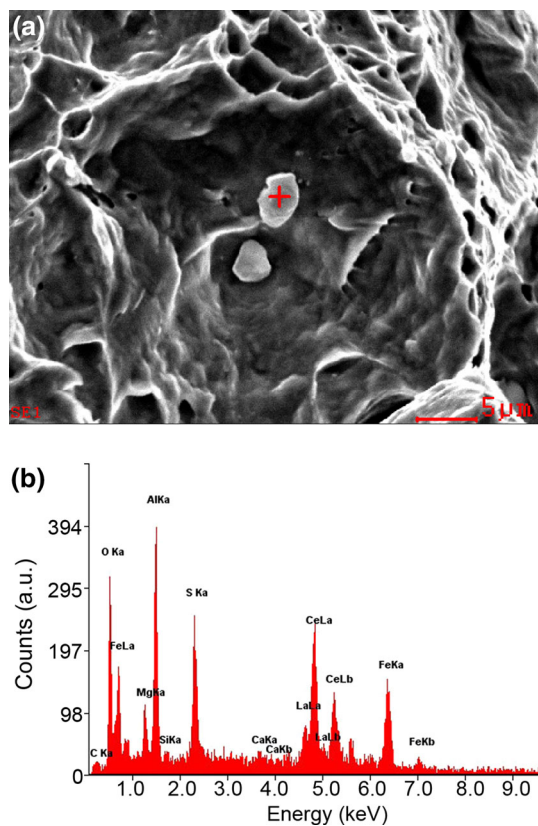
Fig. 8 SEM micrographs of the inclusion located on the fracture **a**, the energy spectrum of the inclusion **b**

Accordingly, it is deduced that the experimental steel has good fire resistance, which is largely associated with the addition of alloying elements, such as Nb, Cu, Ti, and Mo. These alloying elements can form a large amount of MC- and M_2C-type precipitates, which are essentially stable and hardly dissolve at the temperature of 500 °C. The retained precipitation provides a remarkable strengthening for the experimental steel, despite deformation at high temperature. By the pinning effect of fine precipitates, the steel can avoid the fast softening of material in the case of high temperature environment [24].

The Charpy impact energy (A_{KV}) of the steels at processes R1–4 is 27, 27.3, 26.5, and 28 J at room temperature. Correspondingly, the Charpy impact energy is 24, 22.8, 23, and 22.5 J at −20 °C.

Figure 7 shows the SEM micrographs of the impact fracture morphologies, which reveal that all the steels with four different processes perform a typical ductile fracture. Essentially, there is no difference among the morphologies of these fracture surfaces. The dimples on the fracture surface are dense, uniform, and deep enough. Therefore, it can be concluded that the experimental steel has good impact property based on the morphology and number of dimples.

The inclusions located at the center of fracture are analyzed by the energy spectrum, as shown in Fig. 8. The energy spectrum indicates that the inclusions of the steel mainly consist of the oxides or sulfides of Al, Ce, and Mg. These inclusions probably originate from the deoxidizers in steel making and ultimately have a negative effect on impact energy. Hence, the inclusions should be avoided in practical production.

4 Conclusions

(1) The welding crack sensitivity index of the developed steel is 0.146 and the atmospheric corrosion resistance index is 6.06. The activation energy of static recrystallization is 400.9 kJ/mol and the deformation parameter n is 0.2622, 0.3346, and 0.5014, corresponding to 950, 1,000, and 1,050 °C, respectively.

(2) The combined addition of Nb, Ti, Cr, Cu, Mo, and B promotes the bainitic transformation under a low cooling rate so that the range of parameter control is enlarged during TMCP process.

(3) The steel has a microstructure of LB and small amounts of ferrite, and possesses a high strength at both room and elevated temperatures, which originates from the strengthening effect by means of LB transformation, microstructure refinement, and precipitation of alloying elements. The steel shows ductile impact fracture and has average Charpy impact energy of 27.3 and 22.8 J at room temperature and −20 °C, respectively.

(4) The developed steel has a good combination of strength and ductility both at room and elevated temperature, weldability and corrosion resistance, and it can satisfy the basic demands for materials in the manufacture of refuge chamber.

References

[1] X.D. Yang, L.Z. Jin, Appl. Mech. Mater. **170–173**, 1608 (2012)
[2] H. Ghazanfari, M. Naderi, Acta Metall. Sin. (Engl. Lett.) **26**, 635 (2013)
[3] H.F. Fang, S.R. Ge, L.H. Cai, E.Y. Hu, Int. J. Min. Sci. Technol. **22**, 85 (2012)
[4] F.L. Sun, X.G. Li, F. Zhang, X.Q. Cheng, C. Zhou, N.C. Wu, Y.Q. Yin, J.B. Zhao, Acta Metall. Sin. (Engl. Lett.) **26**, 257 (2013)
[5] W. Sheng, M.Z. Gao, L. Yang, Process Eng. **26**, 2351 (2011)
[6] H.J. Zhao, X.M. Qian, J. Li, Saf. Sci. **50**, 674 (2012)

[7] F.G. Caballelo, H.K.D.H. Bhadeshia, K.J.A. Mawella, Mater. Sci. Technol. **17**, 512 (2001)

[8] C.I. Gareia, S.M. Aklis, Mater. Sci. Technol. **13**, 102 (1992)

[9] B.C. Hwang, C.G. Lee, T.H. Lee, Metall. Mater. Trans. A **41**, 85 (2010)

[10] J. Majta, J.G. Lenard, M. Pietrzyk, Mater. Sci. Eng. A **208**, 249 (1999)

[11] W.W. Bose-Filho, A.L.M. Carvalho, M. Strangwood, Mater. Charact. **58**, 28 (2007)

[12] A. Yamamoto, S. Yamauchi, M. Hamada, T. Ikeda, N. Takahashi, U.S. Patent 20,040,129,348, 8 July 2004

[13] Y.L. Shen, R.L. Bodnar, J.Y. Yoo, W.Y. Choo, U.S. Patent 6,187,117 B1, 13 Feb 2001

[14] S.F. Medina, A. Quispe, M. Gómez, Mater. Sci. Technol. **17**, 536 (2001)

[15] H.Y. Wu, L.X. Du, Z.R. Ai, X.H. Liu, J. Mater. Sci. Technol. **29**, 1197 (2013)

[16] S.F. Medina, A. Quispe, ISIJ lnt. **41**, 774 (2001)

[17] S.H. Cho, K.B. Kang, J.J. Jonas, ISIJ Int. **41**, 766 (2001)

[18] Z.Y. Zeng, L.Q. Chen, F.X. Zhu, X.H. Liu, Acta Metall. Sin. (Engl. Lett.) **24**, 381 (2011)

[19] K.Y. Xie, L. Yao, C. Zhu, J.M. Cairney, C.R. Killmore, F.J. Barbaro, J.G. Williams, S.P. Ringer, Metall. Mater. Trans. A **42**, 2199 (2011)

[20] R.D.K. Misra, H. Nathani, J.E. Hartmann, F. Siciliano, Mater. Sci. Eng. A **394**, 339 (2005)

[21] H.J. Jun, J.S. Kang, D.H. Seo, K.B. Kang, C.G. Park, Mater. Sci. Eng. A **422**, 157 (2006)

[22] Z.H. Tang, W. Stumpf, Mater. Sci. Eng. A **490**, 391 (2008)

[23] A. Ghosh, B. Mishra, S. Das, S. Chatterjee, Mater. Sci. Eng. A **374**, 43 (2004)

[24] W.B. Lee, S.G. Hong, C.G. Park, S.H. Park, Metall. Mater. Trans. A **33**, 1689 (2002)